

# ALMA Memo No. 496

## 183 GHz water vapour radiometers for ALMA: Estimation of phase errors under varying atmospheric conditions.

Alison Stirling, Richard Hills, John Richer, Juan Pardo

May 18, 2004

### 1 Abstract

We investigate the use of water vapour radiometers as a tool for estimating phase due to atmospheric water, focusing on the impact of differing atmospheric conditions on the relationship between path length and brightness temperature. We provide a formula for converting between the two for a variety of atmospheric conditions, and outline how the radiometer channel temperatures may be combined to give an optimal estimate for the path difference. This estimate gives an error of about 2% per mm of precipitable water vapour due to atmospheric variations. The presence of hydrometeors such as ice or water droplets is also considered, and we show that radiometers possessing sideband separation could be used to detect the presence of 0.02 mm of column integrated ice for crystals of size  $75\mu\text{m}$ , and about  $10^{-3}$  mm of water droplets.

### 2 Introduction

Astronomical interferometry requires the accurate determination of the path difference between light rays received at different antennas. The path difference, however, contains both information relating to the location of the astronomical source, and contamination from fluctuations in refractive index along the two ray paths. The dominant source of fluctuation occurs in the earth's troposphere, where water vapour and density fluctuations in the air can affect the path length significantly.

The refractive index,  $n$ , of a slab of air can be related to atmospheric water vapour via the Smith-Weintraub equation:

$$N = 77.6\frac{p_d}{T} + 64.8\frac{p_v}{T} + 3.776 \times 10^5 \frac{p_v}{T^2}, \quad (1)$$

where  $N = 10^6 (Re(n) - 1)$ ,  $T$  is the temperature in Kelvin, and  $p_d$  and  $p_v$  are the partial pressures (in mb) of dry air and water vapour respectively. The first two terms give the

contribution to refractivity due to induced dipole transitions, and the third term gives the refractivity due to the permanent dipole moment of water. The wet refractivity term contains a small dispersive component due the extended wings of infrared transitions, and requires an adjustment by about 0.5% at 100 GHz, and 2% at 200 GHz. In this report, we limit our analysis to the non-dispersive contributions to refractivity, and note that dispersion in the context of fast switching for ALMA is discussed in more detail in Holdaway & Pardo (2001).

The partial pressures can be expressed in terms of water vapour and dry air densities using the ideal gas equation:  $p_d = \rho_d RT / \mathcal{M}_d$  and  $p_v = \rho_v RT / \mathcal{M}_v$  where  $\rho_d$  is the density of dry air,  $\rho_v$  the water vapour density;  $R$  is the universal gas constant ( $R = 8.314 \text{ J mol}^{-1} \text{ K}^{-1}$ ), and  $\mathcal{M}_v = 0.01802 \text{ kg mol}^{-1}$ ,  $\mathcal{M}_d = 0.02896 \text{ kg mol}^{-1}$ . This gives

$$N = 77.6 \frac{R\rho_d}{\mathcal{M}_d} + 64.8 \frac{R\rho_v}{\mathcal{M}_v} + 3.776 \times 10^5 \frac{R\rho_v}{\mathcal{M}_v T}. \quad (2)$$

In order to calculate the total path delay,  $L$ , equation 2 is integrated along the line of sight:

$$L = 10^{-6} \int N(y) dy \quad (3)$$

where the units of  $L$  are the same as the units of  $y$ . The path difference between light reaching two antennas is then given by:

$$\Delta L = \int 2.22 \times 10^{-2} \Delta \rho_T + 0.77 \times 10^{-2} \Delta \rho_v + 1.08 \times 10^2 \Delta \left( \frac{\rho_v}{T} \right) dy, \quad (4)$$

where  $\rho_T$  is the total air density, and  $\Delta \rho$  denotes the difference in density along two lines of sight at a given height. Under the hydrostatic approximation, vertical pressure gradients are a function only of the air density,  $\rho_T$ , and so in the absence of horizontal pressure variations this term is zero to first order. However, this approximation breaks down when the atmospheric flow supports vertical accelerations (for example when the flow is turbulent), and the variation in  $\rho_d$  will contribute to the phase fluctuations. The effect of this dry fluctuation term will be considered in another report, and we shall concentrate here on the impact of water vapour fluctuations on the path. The first of the wet terms is small compared with the second, and so the dominant contribution to the phase changes comes from the third term, which varies inversely with temperature. We can therefore see from equation 4 that phase fluctuations depend both on the amount of water vapour present along the line of sight, and on the temperature distribution of this water vapour.

The path fluctuations at the ALMA Chajnantor site, measured on a 300 m baseline are in the range  $50 - 400 \mu\text{m}$  (Evans *et al.* ; 2002). Since the aim is to measure the path per antenna to within  $\{[10(1 + \text{PWV})]^2 + [0.02\Delta L]^2\}^{1/2} \mu\text{m}$  (where PWV is precipitable water vapour in mm), there is a need to correct for the contribution of the water vapour to the path. One method is to point the antennas at a known reference source, from which the atmospheric phase can be deduced. This fast switching technique is discussed in *e.g.* Carilli & Holdaway (1999), and Holdaway (2001). A complementary method is to measure the amount of water vapour along the line of sight using a radiometer operating around the strong water emission line at 183 GHz. The principles of this technique, including the choice of radiometer bands, and the required gain stability are discussed

	Chan. 1	Chan. 2	Chan. 3	Chan. 4
IF/ GHz	0.88	1.94	3.175	5.2
Width/ GHz	0.16	0.75	1.25	2.5

Table 1: Table showing the radiometer bands around the central frequency of 183.31 GHz for the proposed water vapour radiometers.

in Lay (1998); with a model for the phase structure function presented in Carilli, Lay & Sutton (1998). Some preliminary experimental tests have been carried out by *e.g.* Yun & Wiedner, (1999); Delgado *et al.* (2001); and Wiedner *et al.* (2001) who compare interferometric phases measured on a point-like source with the phase retrieved by the radiometer. These tests show that the relationship between water vapour amount and phase can change depending on the prevailing atmospheric conditions. In this memo we concentrate on quantifying the impact of the atmosphere on phase correction for the radiometers designed for the Chajnantor site.

The prototype Chajnantor radiometers have four channels with IFs and band widths given in table 1. There are currently two designs, one with a mechanical Dicke switch to look at a reference load, and the other with a cross correlator which looks simultaneously at the load and the atmosphere. The latter has the possibility of being able to separate the upper and lower side-band frequency channels, which may be used to detect the presence of ice and water droplets. This is discussed in section 6.

We have used an atmospheric radiative transfer code (ATM, Pardo, Cernicharo, & Serabyn; 2001) to model the radiometric response to phase changes given different water vapour and temperature distributions. In section 3 we look at some basic influences on the 183 GHz line profile, and consider the relationship between phase and brightness temperature in section 4. We also measure the spread in sensitivity values from radiosonde data from the Chajnantor site, and in section 5 consider how to combine the estimates of path length from the different radiometer channels. Section 6 considers the response of the radiometers in the presence of ice and water droplets, and a summary is provided in section 7.

### 3 The 183 GHz water vapour line – basic influences

In this section we separate out the influences of different atmospheric properties to show their effect on the 183 GHz water line. We look at the impact of the water vapour amount; the pressure and temperature of the water vapour; the distribution of temperature with height; and the distribution of water vapour with height.

#### 3.1 Water vapour amount

We start by looking at how varying amounts of water vapour change the spectrum around 183 GHz. The tropospheric temperature profile has been given a constant lapse rate of  $\Gamma = -5.6 \text{ K km}^{-1}$ , where

$$T(z) = T_{\text{surface}} + \Gamma z, \quad (5)$$

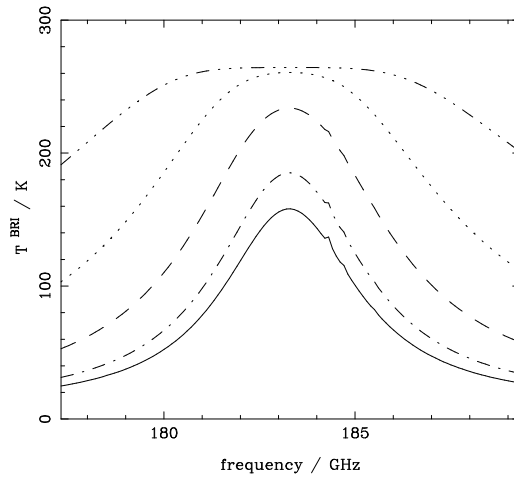


Figure 1: The effect of varying the amount of water vapour in a layer at 1km, with temperature 265 K and pressure 500 mb. Solid line is for 0.5 mm of PWV; dot-dashed for 0.675 mm; dashed for 1.275 mm; dotted, 2.8 mm; and dot-dot-dot-dashed, 6.5 mm.

with surface pressure and temperatures of 560 mb and 270 K. For simplicity the water vapour was placed in a single layer at a height of 1 km and thickness 150 m, and the line profile was calculated for 0.5, 0.675, 1.275, 2.8, and 6.5 mm of precipitable water vapour (PWV). These amounts correspond respectively to the 10, 25, 50, 75, and 90 percentiles of the PWV cumulative function at the Chajnantor site (Evans *et al.* 2002). Figure 1 shows the line profile for the different water vapour amounts, and shows that the line broadens and the brightness temperature increases with increasing water vapour amount until it saturates at about 265K.

### 3.2 Pressure and Temperature

Next we look at how the water vapour line changes with pressure and temperature. The water vapour is placed in a single layer, and to alter the pressure without changing the temperature, we change the height of the layer and set the temperature to be constant with height (*i.e.* an isothermal atmosphere). The temperature is changed while keeping the pressure constant by changing the lapse rate,  $\Gamma$ , but keeping the height of the layer constant. Figure 2 shows how the line changes with pressure and temperature for 1 mm PWV. The left panel shows that the emission line becomes narrower for lower pressures, with two pivot frequencies on either side of the central frequency where the brightness temperature is relatively insensitive to pressure. The right panel of figure 2 shows how the line is affected by the temperature of the water vapour layer. For a 10 K change in temperature of the layer, the brightness temperature changes by less than 5 K. These experiments show that the distribution of water vapour with height is important in determining the shape of the line profile. We will therefore look at how different water vapour and temperature distributions affect the line profile in the next subsection.

### 3.3 Exponential water vapour distributions

To explore the influence of the water vapour distribution on the 183 GHz line profile, we have created a series of water vapour profiles with an exponential distribution and varying scale height. Figure 3 shows that the line is narrowest when there is more water at higher altitudes, where the pressure is lower. This effect diminishes with increasing PWV, when the line starts to saturate.

### 3.4 Varying the lapse rate

Finally we have looked at the brightness temperatures for varying vertical temperature distributions, set by the lapse rate,  $\Gamma$ . Typical values for the lapse rate are  $-5.6$  K/km in moist conditions decreasing to  $-10$  K/km for a very dry atmosphere (this is known as the dry adiabatic lapse rate). The lapse rate can also be affected by turbulent mixing, and surface cooling, both of which tend to make the lapse rate less negative. For these experiments, the water vapour is given an exponential distribution with scale height 2 km. Figure 4 shows that the shape of the line profile is relatively insensitive to the temperature distribution, and that the maximum value decreases by about 2 K in brightness temperature for a 3 K/km increase to the lapse rate.

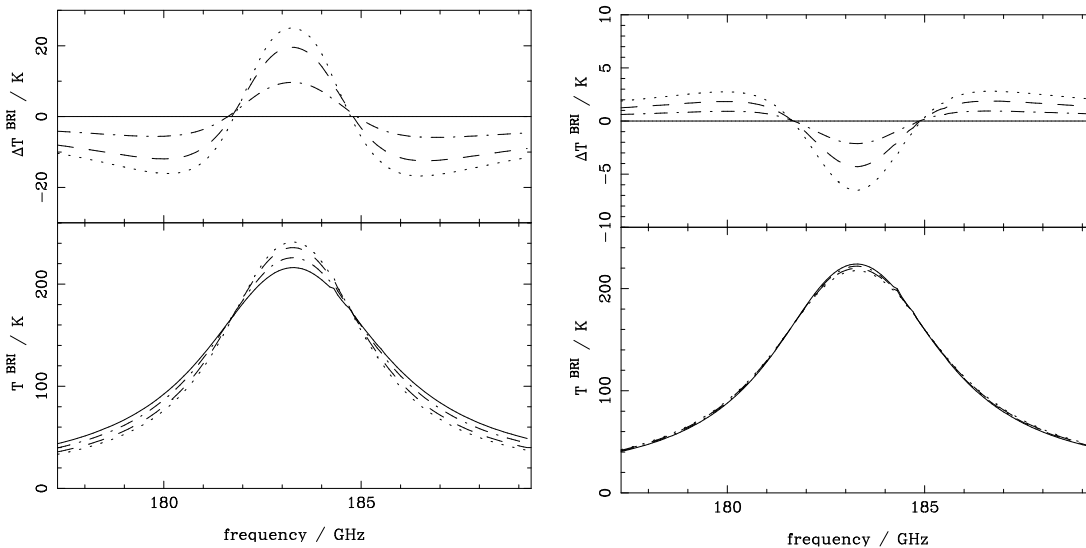


Figure 2: Bottom panels: Left: The effect of changing the pressure of 1 mm PWV at a fixed temperature of 265 K. Solid line is for 560 mb; dot-dashed for 480 mb; dashed 415 mb; and dotted, 375 mb. Right: The effect of changing the temperature of 1 mm PWV at a fixed pressure of 491 mb. Solid line is for 264.2 K; dot-dashed for 260.1 K; dashed, 256.1 K; and dotted, 252.2 K. Top panels show the difference in  $T^{\text{BRI}}$  of each line compared with the solid line.

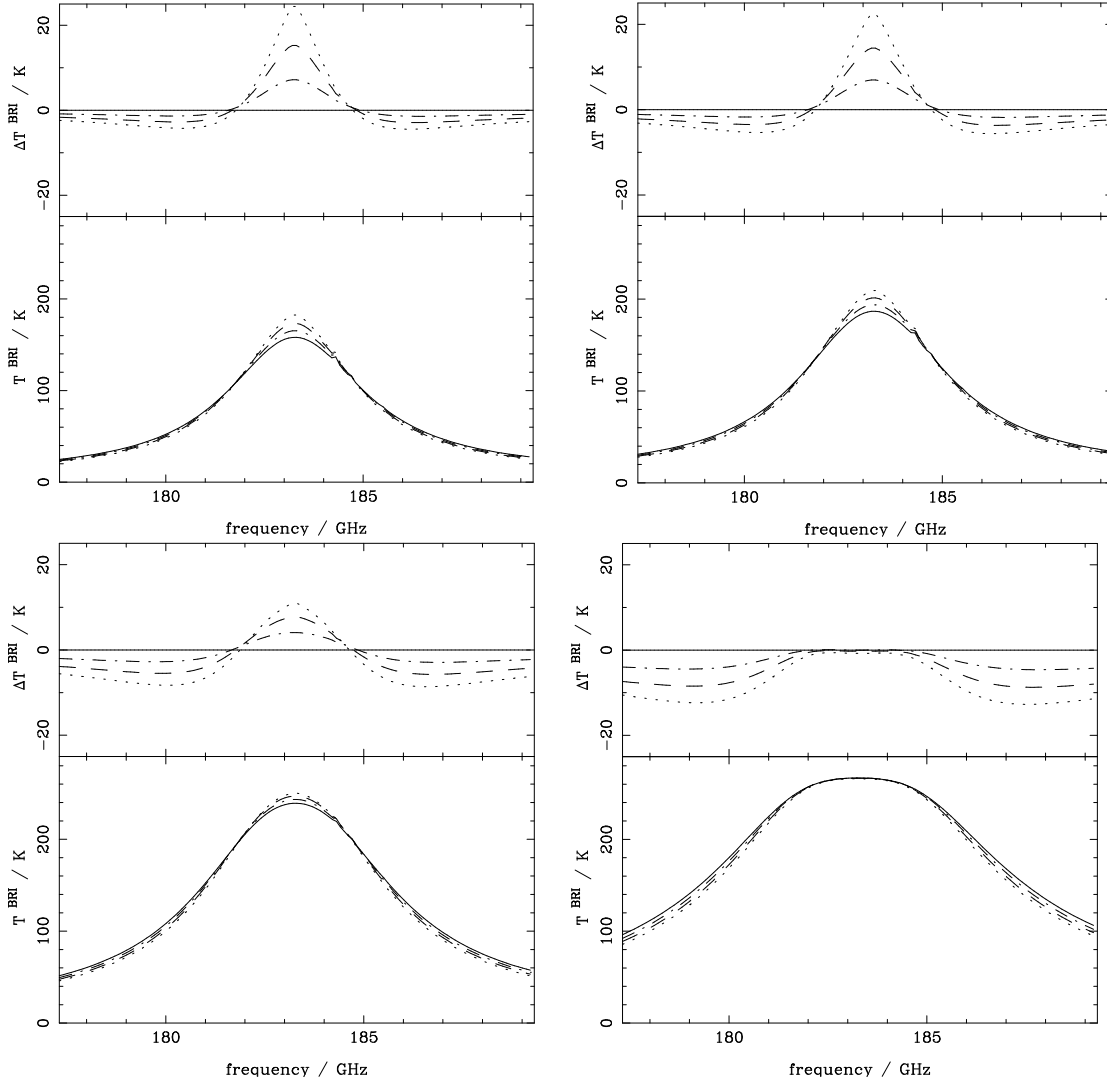


Figure 3: The effect of changing the scale height,  $h_0$ , on the brightness temperature. Top left for  $\text{PWV} = 0.5$ ; top right  $\text{PWV} = 0.675$ ; bottom left  $\text{PWV} = 1.275$ ; bottom right  $\text{PWV} = 2.8$  (representing the 10, 25, 50 and 75 percentile frequency values).  $h_0$  takes the values 0.5, 1.0, 1.5, 2.0 km corresponding to solid, dot-dashed, dashed and dotted lines respectively. The top plots of each panel show the difference in brightness temperature of each line compared with the solid line.

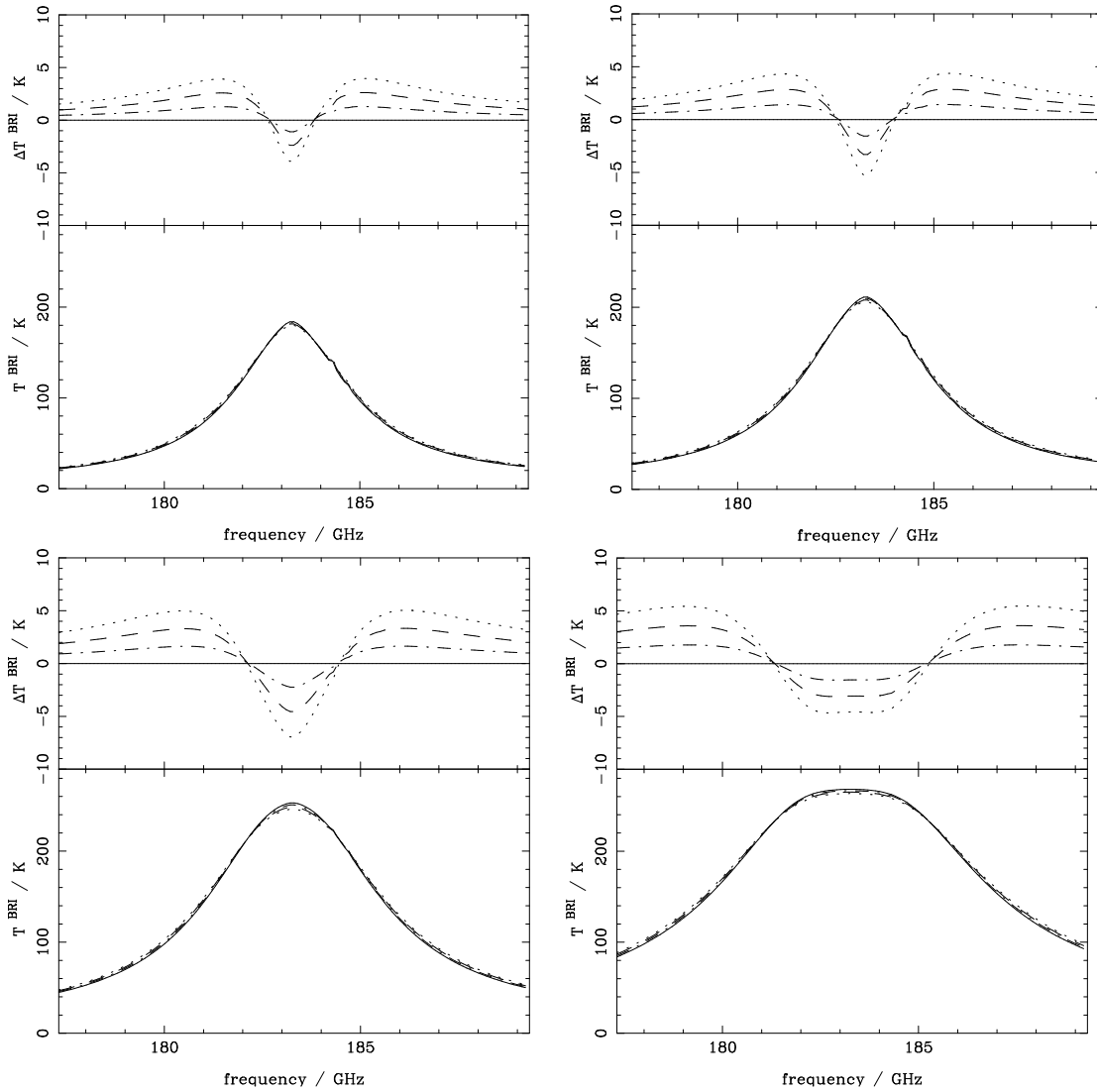


Figure 4: The effect of changing the lapse rate,  $\Gamma$ , on brightness temperature. Top left for PWV = 0.5; top right PWV = 0.675; bottom left PWV = 1.275; bottom right PWV = 2.8 mm (representing the 10,25,50 and 75 percentile frequency values).  $\Gamma$  takes values  $-2.5, -5, -7.5, -10.0$  K/km corresponding to solid, dot-dashed, dashed and dotted lines respectively. The top plots of each panel show the difference in brightness temperature of each line compared with the solid line.

## 4 Radiometric sensitivity to phase for different atmospheric conditions

### 4.1 Introduction

Since our aim is to estimate the path delay from water vapour radiometer measurements, we need to know how the brightness temperature changes for a given change in path length. We can quantify this as a sensitivity parameter,  $dT/dL$ , which is the ratio of brightness temperature change for a given path length change. Clearly, if this sensitivity parameter is constant, then the path difference can be retrieved directly from the brightness temperatures. We expect, however, that the sensitivity parameter will depend on the state of the atmosphere, and this will introduce an error into the estimate of the path difference. If we can quantify this atmospheric dependence, there is scope for limiting this error by measuring relevant atmospheric variables at the site.

In this section we look at making changes to an idealised atmosphere to see how the radiometric sensitivity to path (or  $dT/dL$ ) changes. While water vapour fluctuations are likely to occur over a range of heights, for the following experiments we consider the effect of putting a single fluctuating layer into the atmosphere. This approach allows us to isolate the impact of different atmospheric profiles, and serves as a first step towards understanding the conditions influencing the sensitivity parameter.

### 4.2 Water vapour scale height

We start by looking at how different water vapour scale heights affect the sensitivity parameter,  $dT/dL$ . The tropospheric temperature profile has been set to decrease linearly with height, and the water vapour to decrease exponentially from the ground with a given scale height. In order to measure  $dT/dL$ , a small additional layer of thickness 150 m and containing 0.1 mm of water vapour was placed at a height of 1 km, and we have calculated the difference in brightness temperature with and without this layer for a range of total PWV values. The corresponding change in path length was then calculated to find the ratio  $dT/dL$ . Figure 5 shows how the sensitivity against frequency changes with scale height for a range of total PWV amounts, and figure 6 shows how these values vary with scale height for the four different radiometer channels described in table 1. A 1 km uncertainty in the scale height produces changes in the sensitivity of order a few percent for water vapour amounts between 0.5 and 2.8 mm. We can use these values to infer the uncertainty in the path length for a given measured difference in brightness temperature  $\Delta T^{\text{BRI}}$  as follows:

The corresponding change in path is given by:

$$\Delta L = \frac{\Delta T^{\text{BRI}}}{(dT/dL)}, \quad (6)$$

and the uncertainty in path difference,  $\epsilon(\Delta L)$ , is given by:

$$[\epsilon(\Delta L)]^2 = \frac{\Delta L^2 [\epsilon(dT/dL)]^2 + [\epsilon(\Delta T^{\text{BRI}})]^2}{(dT/dL)^2}, \quad (7)$$

so for large path differences the sensitivity parameter is the dominant contribution to the uncertainty in the path difference and for small  $\Delta L$  the uncertainty in the sensitivity parameter becomes small, and the errors due to noise in the radiometer dominate.

### 4.3 Height of the fluctuating layer

Next we change the height of the additional water vapour layer,  $z_0$ , and use an exponential profile of water vapour with fixed scale height of 1 km. The height of the fluctuating layer is expected to affect the sensitivity for two reasons. Firstly the change in brightness temperature when the layer is higher will be narrower with frequency due to the lower pressure of this layer, and secondly the higher the layer the lower its temperature, and so the greater the path delay contribution.  $dT/dL$  is therefore expected to be lower in amplitude for higher layers, but vary more sharply with frequency around 183.31GHz. Figures 7 and 8 show the resulting sensitivities, with a 1 km uncertainty in the height of the fluctuating layer giving sensitivity changes of between 4 – 10% for water vapour amounts between 0.5 and 2.8 mm.

### 4.4 Lapse rate

In a third numerical experiment the vertical tropospheric temperature distribution was altered by changing the lapse rate, while the water vapour scale height was fixed at 2 km, and the height of the fluctuating layer was placed at 2 km. Figures 9 and 10 show how the sensitivity varies with temperature distribution for linear tropospheric temperature profiles ranging between  $-2.5 \text{ K km}^{-1}$  down to  $-10 \text{ K km}^{-1}$ .

For a  $1 \text{ K km}^{-1}$  uncertainty in the lapse rate, the sensitivity changes typically by less than 1 % for PWV values between 0.5 and 2.8 mm. Since the brightness temperatures are relatively insensitive to the temperature of the fluctuating layer, but the path delay is proportional to  $T^{-1}$ , we can convert these results into a dependence of  $dT/dL$  on the temperature of the fluctuating layer. For this we find that the uncertainty in the path length is again of order 1 % per Kelvin for 0.5 – 2.8 mm PWV.

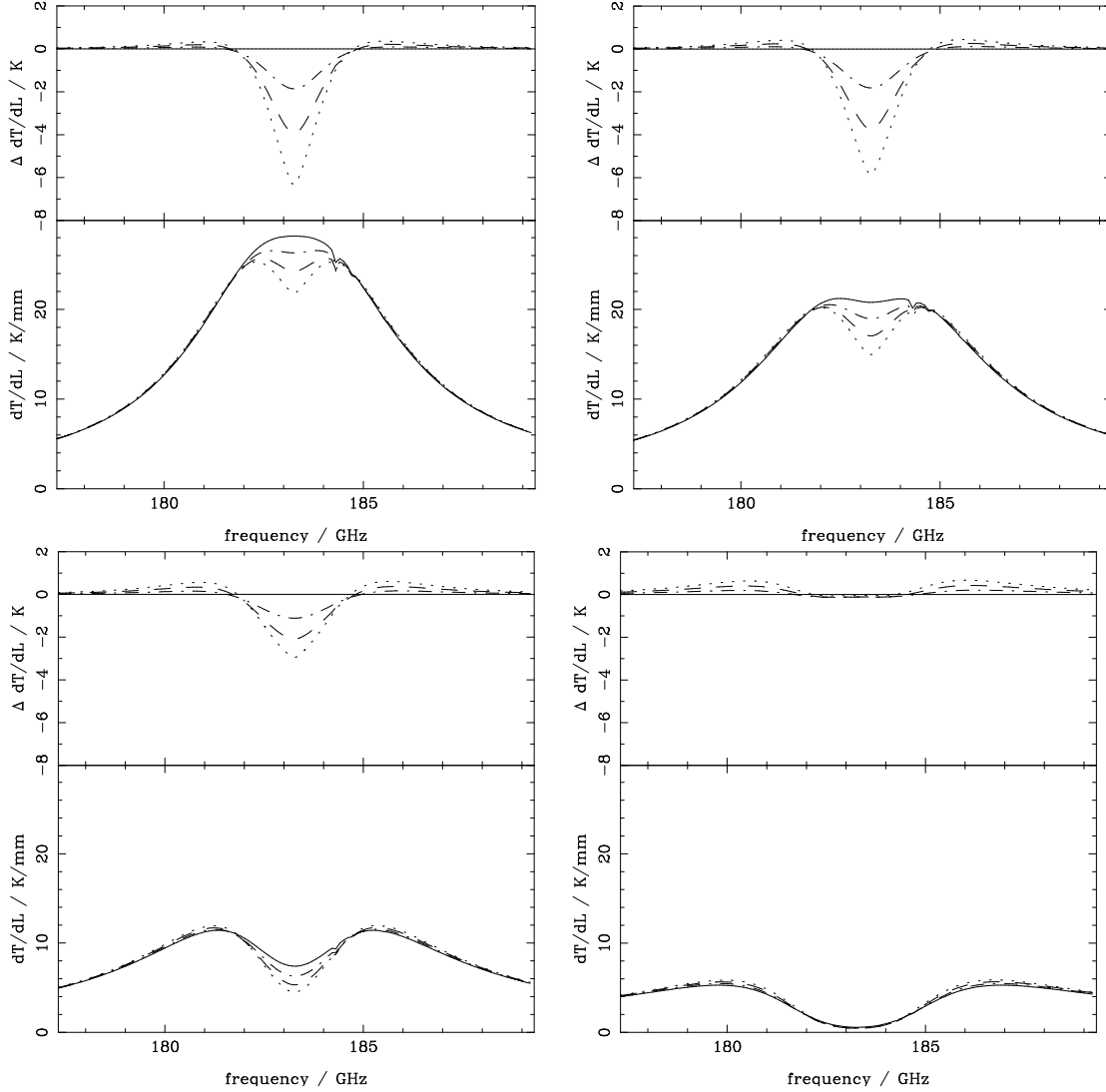


Figure 5: The effect of changing the scale height,  $h_0$ , on the brightness temperature. Top left for  $PWV = 0.5$ ; top right  $PWV = 0.675$ ; bottom left  $PWV = 1.275$ ; bottom right  $PWV = 2.8$  mm (representing the 10, 25, 50 and 75 % frequency values).  $h_0$  takes the values 0.5, 1.0, 1.5, 2.0 km corresponding to solid, dot-dashed, dashed and dotted lines respectively. The top plots of each panel show the difference in brightness temperature of each line compared with the solid line.

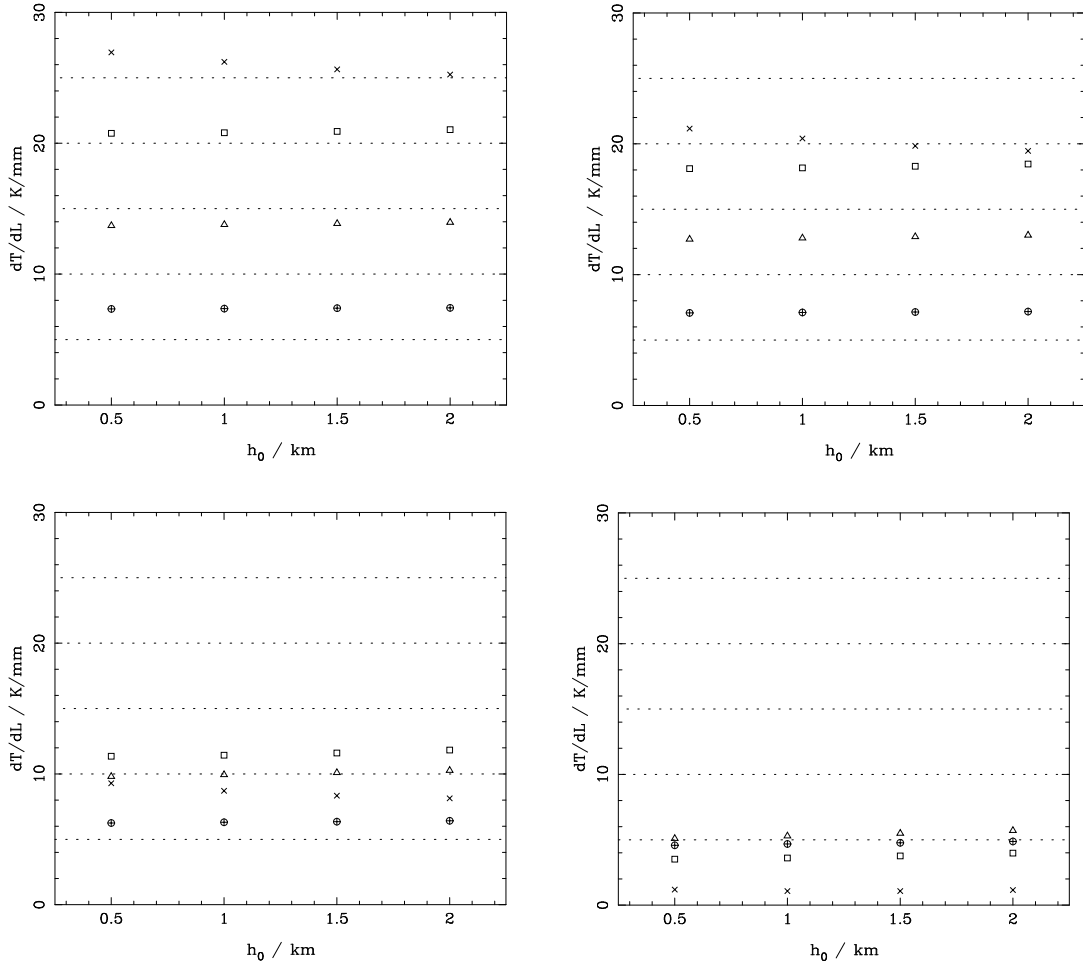


Figure 6: The effect of changing the scale height,  $h_0$ , on the radiometer channel sensitivity,  $dT/dL$ . Top left for  $PWV = 0.5$ ; top right  $PWV = 0.675$ ; bottom left  $PWV = 1.275$ ; bottom right  $PWV = 2.8$  mm (representing the 10,25,50 and 75 % frequency values). Crosses correspond to channel 1, squares to channel 2, triangles to channel 3 and circles to channel 4.

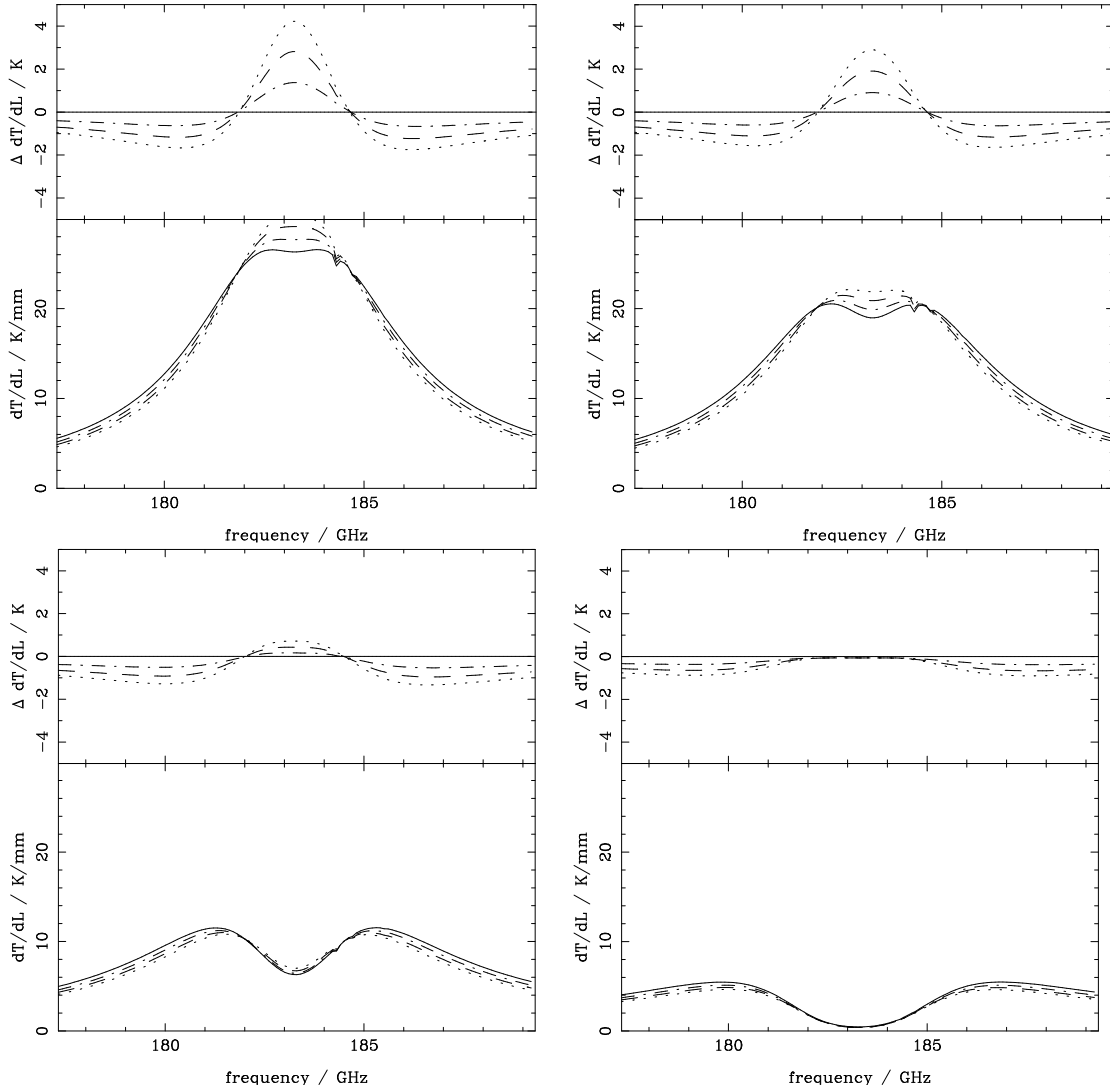


Figure 7: The effect of changing the height of the fluctuating layer,  $z_0$  on the sensitivity parameter,  $dT/dL$ . Top left for PWV = 0.5; top right PWV = 0.675; bottom left PWV = 1.275; bottom right PWV = 2.8 mm (representing the 10, 25, 50 and 75 % frequency values).  $z_0$  takes the values 0.5, 1.0, 1.5, 2.0 km above ground level, corresponding to solid, dot-dashed, dashed and dotted lines respectively. The top plots of each panel show the difference in  $dT/dL$  of each line compared with the solid line.

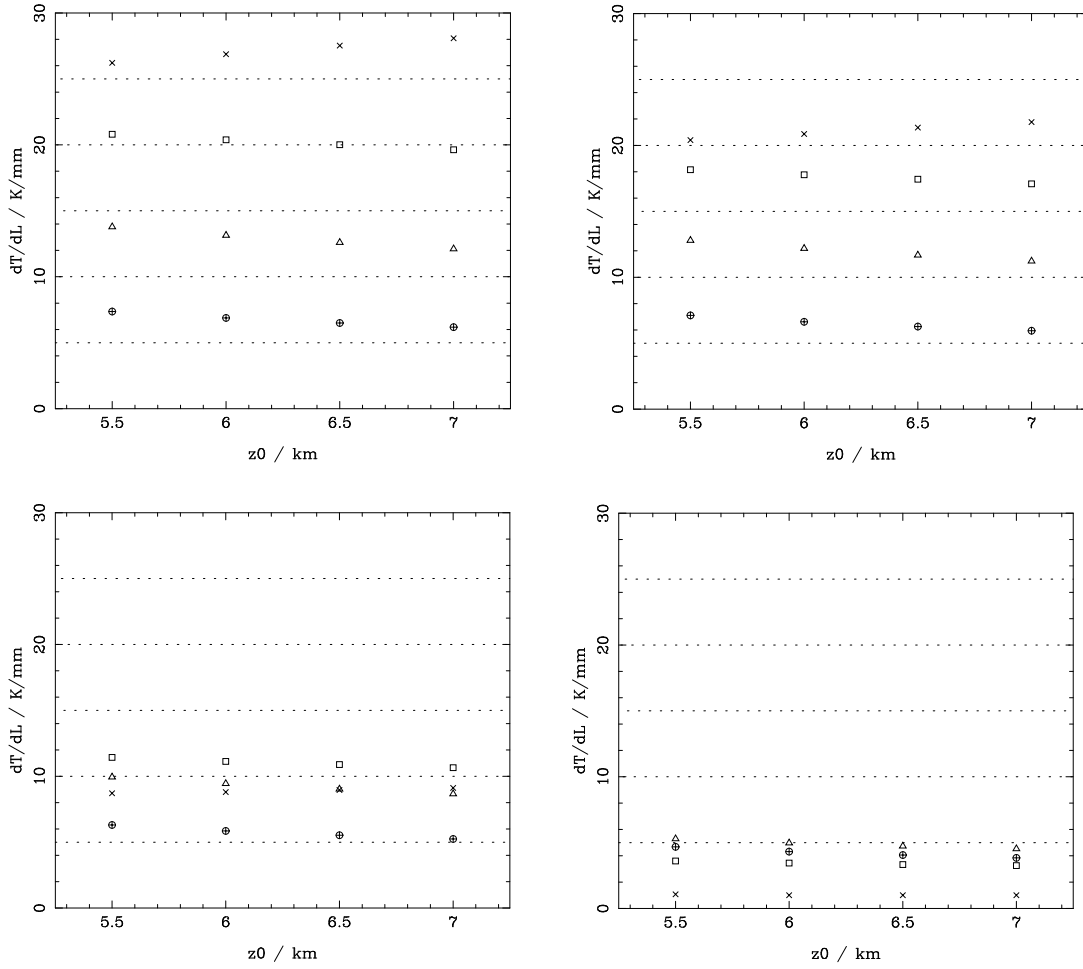


Figure 8: The effect of changing the height of the fluctuating layer,  $z_0$  on the radiometer channel sensitivity,  $dT/dL$ . Top left for  $PWV = 0.5$ ; top right  $PWV = 0.675$ ; bottom left  $PWV = 1.275$ ; bottom right  $PWV = 2.8$  mm (representing the 10, 25, 50 and 75 % frequency values). Crosses correspond to channel 1, squares to channel 2, triangles to channel 3 and circles to channel 4.

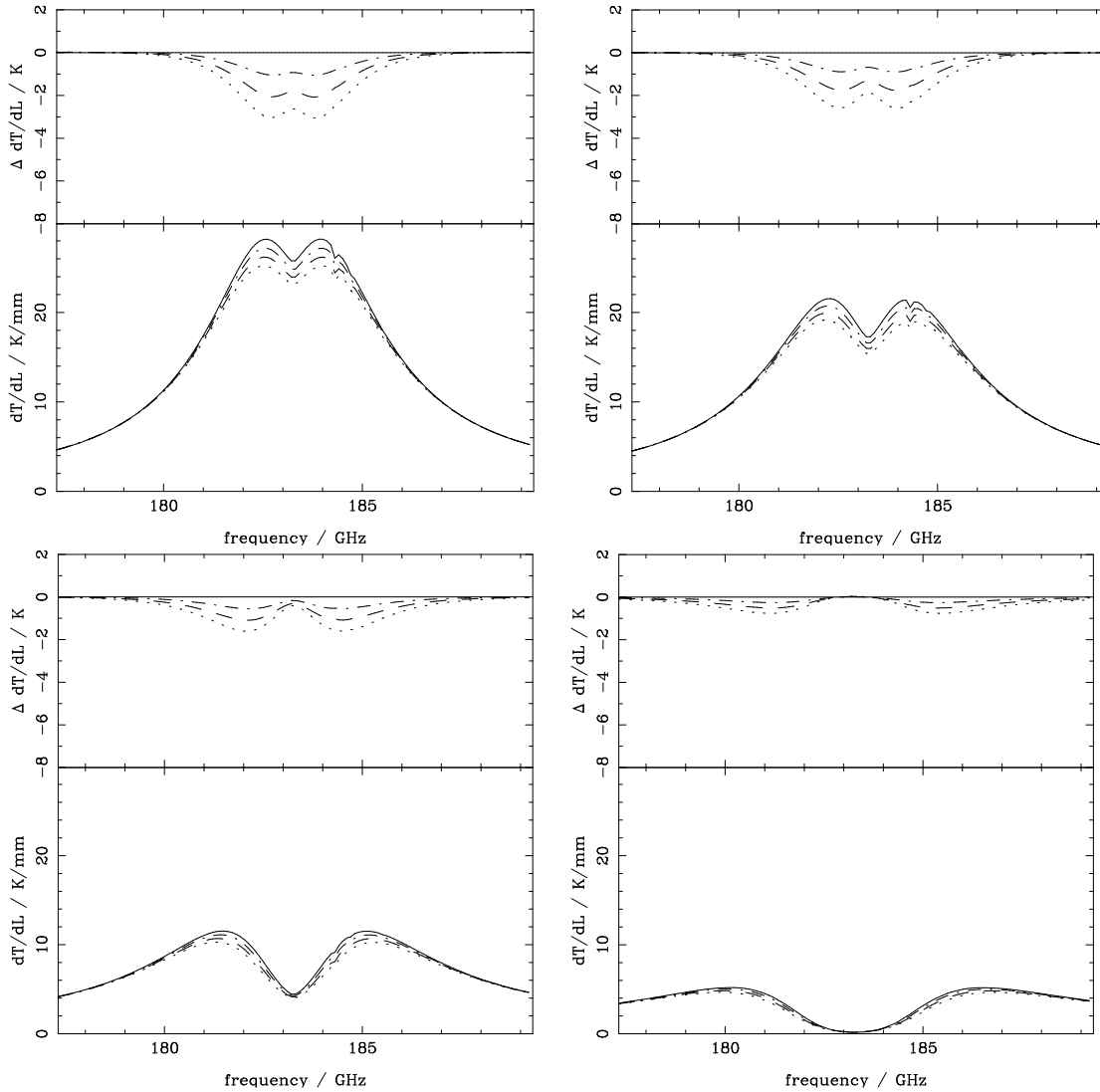


Figure 9: The effect of changing the lapse rate,  $\Gamma$ , on the sensitivity  $dT/dL$ . Top left for  $PWV = 0.5$ ; top right  $PWV = 0.675$ ; bottom left  $PWV = 1.275$ ; bottom right  $PWV = 2.8$  mm (representing the 10,25,50 and 75 % frequency values).  $\Gamma$  takes values -2.5, -5, -7.5, -10. K/km corresponding to solid, dot-dashed,dashed and dotted lines respectively.

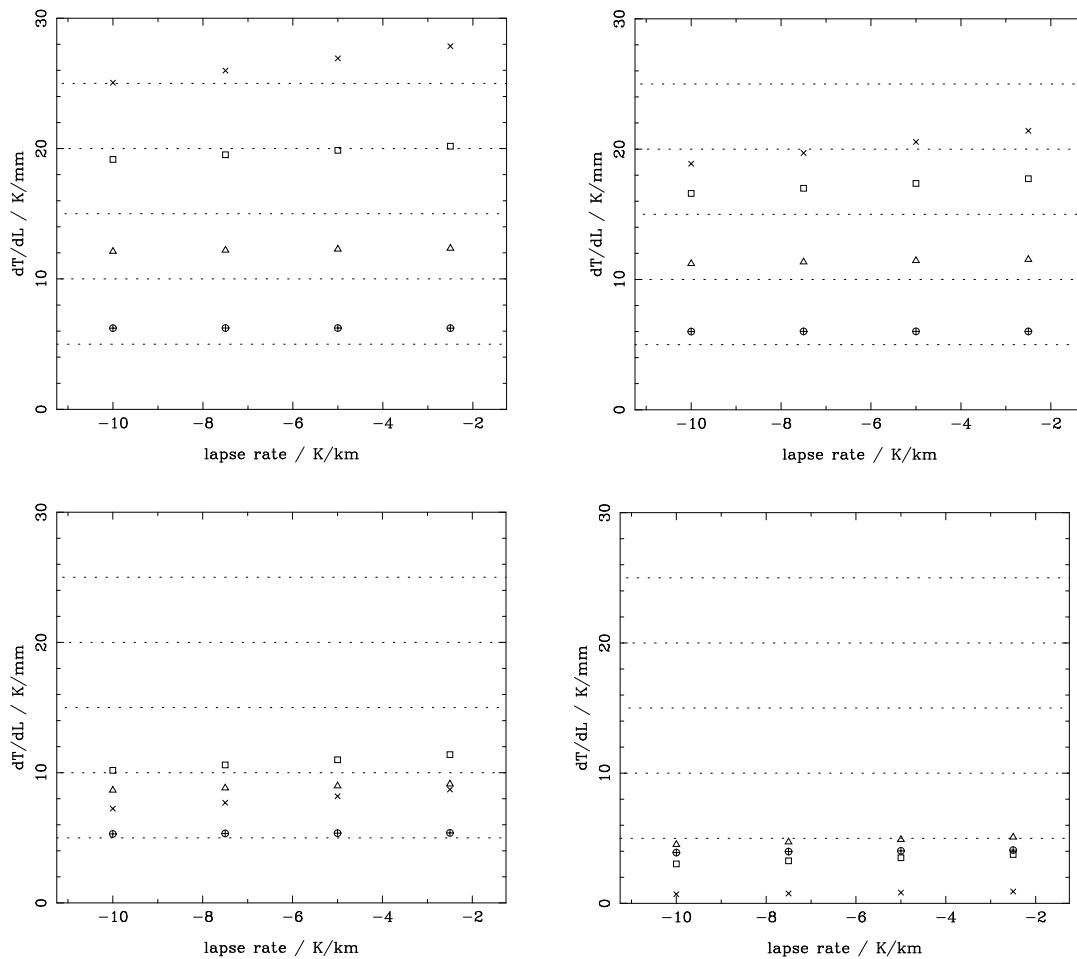


Figure 10: The effect of changing the lapse rate,  $\Gamma$ , on the radiometer channel sensitivity,  $dT/dL$ . Top left for  $PWV = 0.5$ ; top right  $PWV = 0.675$ ; bottom left  $PWV = 1.275$ ; bottom right  $PWV = 2.8$  mm (representing the 10,25,50 and 75 % ile frequency values). Crosses correspond to channel 1, squares to channel 2, triangles to channel 3 and circles to channel 4.

## 4.5 Combining results

Since the sensitivity parameter  $dT/dL$  appears to have a linear dependence on  $z_0$ ,  $h_0$  and  $\Gamma_0$ , we can combine the results from the previous sections to produce a linear fitted formula for  $dT/dL$  as a function of  $z_0$ ,  $h_0$  and  $\Gamma_0$  for the different channels and for different amounts of PWV. This will enable us to estimate the uncertainty in  $dT/dL$  depending on the constraints we can provide for  $z_0$ ,  $h_0$  and  $\Gamma_0$ . Assuming  $dT/dL$  can be parametrised with a linear fit in each of the three directions  $z_0$ ,  $h_0$  and  $\Gamma_0$ , we can write  $dT/dL$  as:

$$\frac{dT}{dL} = axyz + bxy + cxz + dyz + ex + fy + gz + h, \quad (8)$$

where  $a - h$  are constants, and

$$x = \frac{h_0 - h_0^{\min}}{h_0^{\max} - h_0^{\min}}; \quad y = \frac{\Gamma_0 - \Gamma_0^{\min}}{\Gamma_0^{\max} - \Gamma_0^{\min}}; \quad z = \frac{z_0 - z_0^{\min}}{z_0^{\max} - z_0^{\min}} \quad (9)$$

and

$$\begin{aligned} h_0^{\min} &= 0.5 \text{ km}; & \Gamma_0^{\min} &= -10.0 \text{ K km}^{-1}; & z_0^{\min} &= 0.5 \text{ km} \\ h_0^{\max} &= 2.0 \text{ km}; & \Gamma_0^{\max} &= -2.5 \text{ K km}^{-1}; & z_0^{\max} &= 2.0 \text{ km}. \end{aligned} \quad (10)$$

The coefficients  $a - h$  can be found by calculating the sensitivity parameter for a cube of 8  $(x, y, z)$  values, each taking values 0 and 1, and where  $x, y, z$  are defined in equation 9. The coefficients have been calculated for each of the channels and a range of PWV amounts, and the values are summarised in table 2.

We can also express the uncertainty in the sensitivity parameter in terms of the uncertainty in the values of the scale height, lapse rate, and height of the fluctuating layer. Assuming that these quantities vary independently, the uncertainty can be expressed as:

$$\begin{aligned} \left[ \epsilon \left( \frac{dT}{dL} \right) \right]^2 &= [\epsilon(x)]^2 \left( \frac{\partial \frac{dT}{dL}}{\partial x} \right)_{y,z}^2 + [\epsilon(y)]^2 \left( \frac{\partial \frac{dT}{dL}}{\partial y} \right)_{x,z}^2 + [\epsilon(z)]^2 \left( \frac{\partial \frac{dT}{dL}}{\partial z} \right)_{x,y}^2 \\ &= [\epsilon(x)]^2 (ayz + by + cz + e)^2 + \\ &\quad [\epsilon(y)]^2 (axz + bx + dz + f)^2 + \\ &\quad [\epsilon(z)]^2 (axy + cx + dy + g)^2. \end{aligned} \quad (11)$$

We can now estimate the total expected uncertainty in  $dT/dL$  for each channel. Firstly we have estimated the uncertainty in lapse rate and scale height from 200 radiosonde ascents (Radford *et al.*, 2003) taken over a period of four years at Chajnantor. This gave values for the scale height and lapse rate of  $\Gamma_0 = -6.8 \pm 1.5 \text{ K km}^{-1}$ , and  $h_0 = 1.5 \pm 1.0 \text{ km}$ . For the height of the fluctuating layer, we have used a value from Robson *et al.* (2000), who found  $z_0 = 0.4 \pm 0.3 \text{ km}$  during their observing run. Table 3 shows the expected sensitivity values, and their associated uncertainty, which is generally in the range 2 – 5%. It is worth noting at this stage that these values assume that the PWV is well known. Clearly an uncertainty in the PWV will increase the uncertainty in  $dT/dL$ , and this will be considered in more detail in a later report.

Since the parametrisation for  $dT/dL$  in equation 8 makes the assumption that the water vapour is exponentially distributed and that the temperature decreases linearly with

PWV/mm	Channel	$a$	$b$	$c$	$d$	$e$	$f$	$g$	$h$
0.50	1	0.69	0.37	-1.16	1.14	-1.88	0.59	1.50	26.59
0.50	2	0.21	0.36	-0.27	0.17	0.07	0.28	-1.23	20.59
0.50	3	0.05	0.14	-0.07	-0.06	0.16	0.10	-1.63	13.65
0.50	4	0.01	0.04	-0.00	-0.07	0.06	0.02	-1.16	7.33
0.68	1	0.77	0.27	-1.28	0.96	-1.83	0.54	1.14	20.84
0.68	2	0.26	0.41	-0.34	0.16	0.11	0.30	-1.10	17.92
0.68	3	0.07	0.18	-0.09	-0.05	0.20	0.11	-1.53	12.64
0.68	4	0.01	0.05	-0.00	-0.07	0.07	0.02	-1.13	7.06
1.27	1	0.79	-0.18	-1.27	0.52	-1.01	0.34	0.44	9.09
1.27	2	0.36	0.40	-0.47	0.14	0.24	0.31	-0.76	11.17
1.27	3	0.11	0.25	-0.14	-0.03	0.32	0.16	-1.24	9.71
1.27	4	0.02	0.08	-0.01	-0.06	0.12	0.04	-1.03	6.22
2.80	1	0.47	-0.43	-0.69	0.11	0.23	0.06	0.02	1.15
2.80	2	0.38	0.10	-0.51	0.07	0.42	0.18	-0.30	3.41
2.80	3	0.17	0.24	-0.23	-0.01	0.47	0.17	-0.72	5.00
2.80	4	0.04	0.12	-0.03	-0.04	0.22	0.07	-0.83	4.54

Table 2: Table showing the parameters required to obtain  $dT/dL$  as a function of scale height, fluctuating layer height, and lapse rate. Parameters  $a, b, c, d, e, f, g, h$  are defined in equations 8 and 9, and have units  $\text{K mm}^{-1}$ .

PWV/mm	Chan. 1/ $\text{K mm}^{-1}$	Chan. 2/ $\text{K mm}^{-1}$	Chan. 3/ $\text{K mm}^{-1}$	Chan. 4/ $\text{K mm}^{-1}$
0.50	25.58 +/- 1.20	20.95 +/- 0.31	13.95 +/- 0.37	7.47 +/- 0.24
0.68	19.85 +/- 1.17	18.32 +/- 0.32	12.98 +/- 0.37	7.21 +/- 0.24
1.27	8.50 +/- 0.72	11.65 +/- 0.36	10.16 +/- 0.40	6.41 +/- 0.24
2.80	1.23 +/- 0.08	3.83 +/- 0.36	5.52 +/- 0.44	4.81 +/- 0.25

Table 3: Table showing the expected values and uncertainties of  $dT/dL$  for typical uncertainties in  $\Gamma_0, h_0$  and  $z_0$ . ( $\Gamma_0 = -6.8 \pm 1.5 \text{ K km}^{-1}$ ,  $h_0 = 1.5 \pm 1.0 \text{ km}$ , and  $z_0 = 0.4 \pm 0.3 \text{ km}$ ).

height, it is worth comparing our prediction with  $dT/dL$  measured from real atmospheric data from the Chajnantor site. Again we use the 200 radiosonde data profiles to provide realistic water vapour and temperature profiles. The locations of the fluctuating layers of water vapour are not readily obtained from single radiosonde ascents, so for comparison we have used the same approach as the earlier experiments, and inserted an additional water vapour layer of 0.1 mm at 1 km and thickness 150 m to represent the fluctuating layer, and calculated the brightness temperature change due to this layer, along with the associated change in path length. Since  $z_0$  has been held constant for the above analysis, we set  $\epsilon(z) = 0$  for this comparison. Figure 11 shows the predicted  $dT/dL$  values with associated errors from equations 8 and 11, with the values found for the radiosonde ascents overlaid. There is good agreement between our parametrised fit and the radiosonde data, suggesting that the use of a linear fit to  $dT/dL$ , and the assumptions of exponential water vapour profiles with constant lapse rates are reasonable approximations to make.

Clearly it is desirable to minimise our uncertainty in the values of  $\Gamma_0, h_0$ , and  $z_0$ , and this may to a large part be achieved by using a separate instrument to measure the temperature profile. While the temperature profile will give a much better estimate for  $\Gamma_0$ , it may also

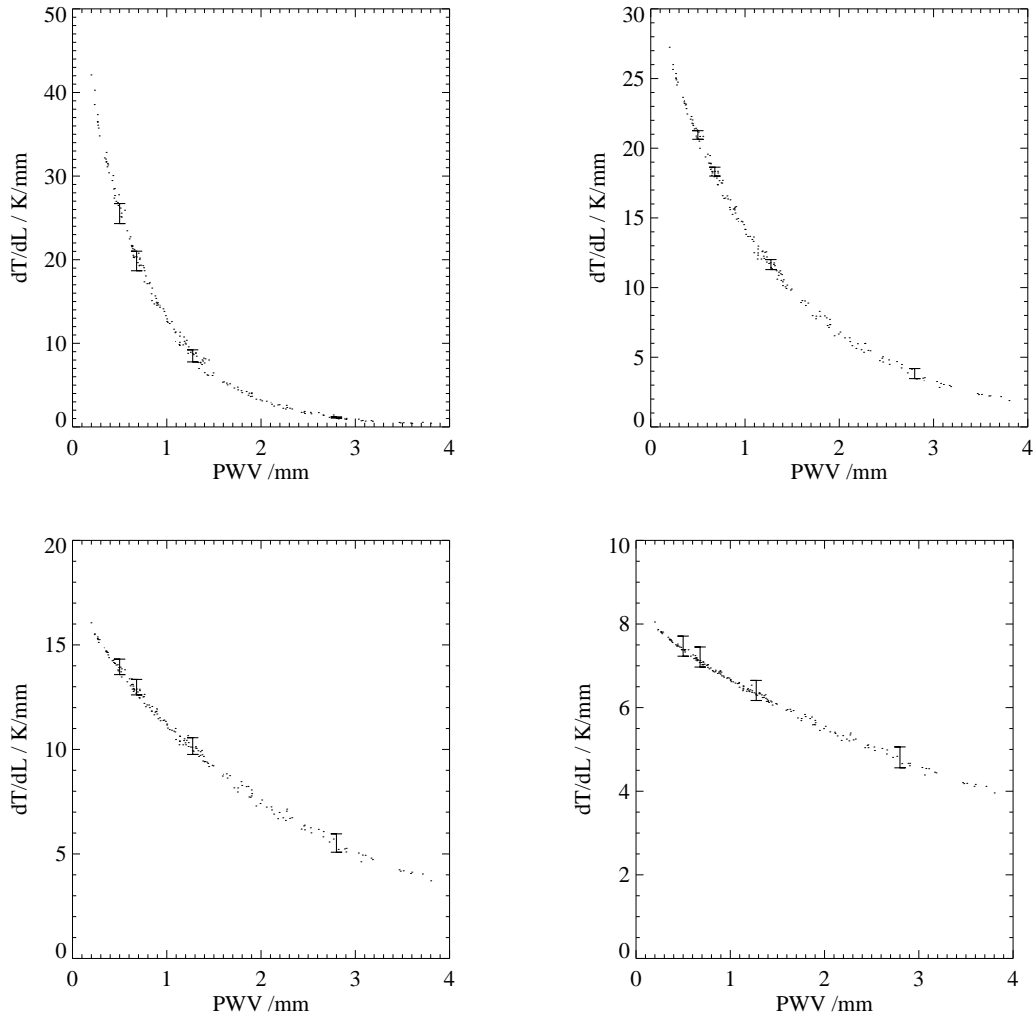


Figure 11: Comparison of  $dT/dL$  measured from radiosonde ascents with associated predictions. Each point represents  $dT/dL$  calculated from a radiosonde profile, and error bars show the predictions from equations 8 and 11. Top left is for channel 1, top right for channel 2, bottom left for channel 3, bottom right for channel 4.

provide information relating to  $h_0$  and  $z_0$ . One example of where  $h_0$  and  $z_0$  may be linked to the temperature profile is in the presence of a temperature inversion. This tends to prevent air from below mixing with air from above the inversion, and so the transport of water vapour upwards is also curtailed. The extent of the water vapour distribution then tends to be set by the height of the inversion. In cases where the water vapour profile experiences a sharp cut off at a given height, very slight vertical mixing can give rise to a high difference in water vapour amount at that height, and so the fluctuating layer of water vapour is most likely also to be set by the height of the inversion. We are currently investigating how often, and how reliably one can obtain information about the water vapour profile from the temperature profile.

One instrument that would be able to measure the temperature profile is a seven-channel radiometer that measures emission from oxygen lines between 51–59 GHz. Typically these oxygen radiometers can measure temperature profiles with an r.m.s. error of less than 1 K up to 1 km above ground level, increasing to 1.5 K at 6 km. There is some uncertainty about the vertical resolution of such an instrument, and in particular it may not resolve higher level temperature inversions, which could increase the uncertainty in temperature to about 3 K at an inversion. The dominant water vapour fluctuations, however, are expected to be concentrated at lower levels where inversions are better represented. In this case, the instrument could allow us to reduce the uncertainty in path due to temperature to about 1%.

## 5 Combining path estimates from the different channels

Now that we have modelled the relationship between brightness temperature and path length, we can take an initial look at the question of how best to combine the values being produced by the four channels of the radiometer. In general this will be done by taking the temperature from each channel, subtracting from it some reference value, so we have the fluctuation in the temperature, and then dividing by the sensitivity parameter ( $dT/dL$ ) to get the corresponding path fluctuation. (The reference value might be the average temperature for that channel over all the radiometers on the array, or a value taken from the most recent observation of a calibrator.) We will then have four estimates of the path fluctuation. If there were no noise on the data and our model were perfect, these should be identical. Since there will be both noise in the data and uncertainty in the model, they will not agree and we need to find the best way of combining them. The simplest thing to do is to form a weighted average of the four values of the path fluctuation.

In the case where the fluctuations are small, our main concern is to minimise the errors introduced by the noise and residual gain fluctuations in the radiometer. The procedure in this case is straight-forward: we estimate the errors expected in the individual channels and convert these into errors in the path. Assuming these errors to be independent, which should be true so long as noise dominates, we can then use the standard result that the weights should be inversely proportional to the squares of the errors. Table 5 gives examples of this. For details of the noise estimates see Hills (2004).

As the fluctuations become larger we become less concerned about the noise and more concerned about the accuracy of the conversion, as discussed in the previous section. As

PWV / mm	Channel 1 / $\mu\text{m}$	Channel 2 / $\mu\text{m}$	Channel 3 / $\mu\text{m}$	Channel 4 / $\mu\text{m}$
0.5	10.9	6.7	9.6	17.7
0.68	14.1	7.3	9.6	17.4
1.27	34.1	11.3	10.3	16.3
2.8	247.8	41.3	19.7	15.4

Table 4: Expected errors in retrieved path due to noise for each radiometer channel for a range of PWV values. ( $\epsilon_{B_i}/\{dT/dL\}$ )

an extreme case we could choose a set a weights such that the average is independent of these various parameters. Another approach is to incorporate the uncertainty in  $dT/dL$  into the path error estimate having weighted the channels with one over the radiometer noise squared. We outline this method below.

Let  $B_i = \Delta T_i^{\text{BRI}}$  *i.e.* the measured brightness temperature change in channel  $i$ , with an error due to radiometer noise,  $\epsilon_{B_i}$  (see table 4). For ease of notation we call the sensitivity parameter for channel  $i$   $S_i \equiv dT/dL$ , which is a function of the atmospheric variables  $x, y, z$  (defined in equation 9) which are allowed to vary independently. The sensitivity parameter has errors associated with the uncertainties in the atmospheric parameters  $x, y, z$ , and we call these  $\epsilon_{S_i^x}, \epsilon_{S_i^y}, \epsilon_{S_i^z}$  respectively.

The path difference,  $\Delta L_i$ , as measured in channel  $i$  is then given by

$$\Delta L_i = B_i/S_i. \quad (12)$$

We first construct weights for finding an optimal estimate for the path from the four channels assuming there is no error in  $S_i$ :

$$\Delta L = \sum_i \frac{\hat{w}_i B_i}{S_i}, \quad (13)$$

where

$$w_i = \frac{S_i^2}{\epsilon_{B_i}^2}; \text{ and } \quad \hat{w}_i = \frac{w_i}{\sum_i w_i}. \quad (14)$$

The error in path due to the radiometer noise is given by:

$$(\epsilon_{\Delta L_{\text{noise}}})^2 = \sum_i \frac{\hat{w}_i^2 \epsilon_{B_i}^2}{S_i^2} = \frac{1}{\sum_i w_i}, \quad (15)$$

and some examples for this are shown in table 5.

We can add in the contribution to path error from uncertainties in  $dT/dL$  as follows: First consider the error introduced into  $\Delta L$  by an uncertainty in the parameter  $x$ . So now  $x \rightarrow x \pm \Delta x$ , and  $\epsilon_{S_i^x} = S_i(x + \Delta x) - S_i(x)$ . So now the error in the path difference due to uncertainty in  $x$  is:

$$\epsilon_{\Delta L_x} = \sum_i \frac{w_i B_i}{S_i(\Delta x + x)} - \frac{w_i B_i}{S_i(x)} \simeq \sum_i \frac{w_i B_i \epsilon_{S_i^x}}{S_i^2}. \quad (16)$$

PWV /mm	$\hat{w}_1$	$\hat{w}_2$	$\hat{w}_3$	$\hat{w}_4$	$\epsilon_{\Delta L_{\text{noise}}}$ / $\mu\text{m}$	$\epsilon_{\Delta L_{x,y,z}}$ / $\mu\text{m}$	$\epsilon_{\Delta L_{\text{Total}}}$ / $\mu\text{m}$
0.5	0.188	0.496	0.245	0.071	4.7	5.2	7.0
0.68	0.132	0.494	0.287	0.087	5.1	6.4	8.2
1.27	0.039	0.359	0.359	0.171	6.7	12.5	14.2
2.8	0.002	0.080	0.348	0.570	11.6	25.2	27.7
0.5	0.233	0.607	0.153	0.007	5.0	4.3	6.6
0.68	0.212	0.602	0.177	0.009	5.6	4.9	7.4
1.27	0.180	0.451	0.451	0.095	8.6	7.8	11.6
2.8	0.003	-0.019	0.091	0.924	14.4	21.5	25.8

Table 5: The channel weights required to minimise the path error due to noise ( $\hat{w}_i$ ) and associated estimate for this path error,  $\epsilon_{\Delta L_{\text{noise}}}$ ; an estimate of the error due to uncertainty in the conversion factor,  $\epsilon_{\Delta L_{x,y,z}}$ ; and estimate for the total combined path error  $\epsilon_{\Delta L_{\text{Total}}}$ . These values have been obtained assuming a total path difference,  $\Delta L$ , of 400  $\mu\text{m}$ . Top half of table uses weights from equation 14, bottom half of table shows how these estimates change when the weights are reoptimised to minimise the total path error.

The total error in the path difference due to uncertainties in  $x$ ,  $y$ , and  $z$  can be found by adding  $\epsilon_{\Delta L_{x,y,orz}}$  in quadrature:

$$\left(\epsilon_{\Delta L_{x,y,z}}\right)^2 = \left(\epsilon_{\Delta L_x}\right)^2 + \left(\epsilon_{\Delta L_y}\right)^2 + \left(\epsilon_{\Delta L_z}\right)^2. \quad (17)$$

The total error in path is then found by combining the error due to radiometer noise and the error due to uncertainties in  $x$ ,  $y$ ,  $z$ :

$$\left(\epsilon_{\Delta L_{\text{Total}}}\right)^2 = \left(\epsilon_{\Delta L_{\text{noise}}}\right)^2 + \left(\epsilon_{\Delta L_{x,y,z}}\right)^2. \quad (18)$$

Finally, since the weights  $\hat{w}_i$  were chosen to minimise the error in the noise alone, we can adjust these using a suitable optimisation procedure to give weights that minimise the total error. This approach is illustrated in table 5, which gives the final error estimate with and without the adjusted weights. It can be seen that the modification in weights only reduces the path error by a few percent. Figure 12 shows how the path error is expected to change with PWV for the values in table 5, with this method enabling a retrieval of path difference with an error of given by:

$$\epsilon_{\Delta L_{\text{Total}}} = \left\{ [3.7(1 + \text{PWV})]^2 + [0.02\Delta L \text{PWV}]^2 \right\}^{\frac{1}{2}} \mu\text{m} \quad (19)$$

where the first term is due to radiometer noise, and the second is due to uncertainties in atmospheric parameters. While this is an encouraging result, it should be noted that there are number of additional sources of error to consider, for example uncertainty in PWV; water vapour fluctuations distributed over a range of heights; and radiometer calibration errors. Future work will concentrate on broadening this analysis to take account of the more general case.

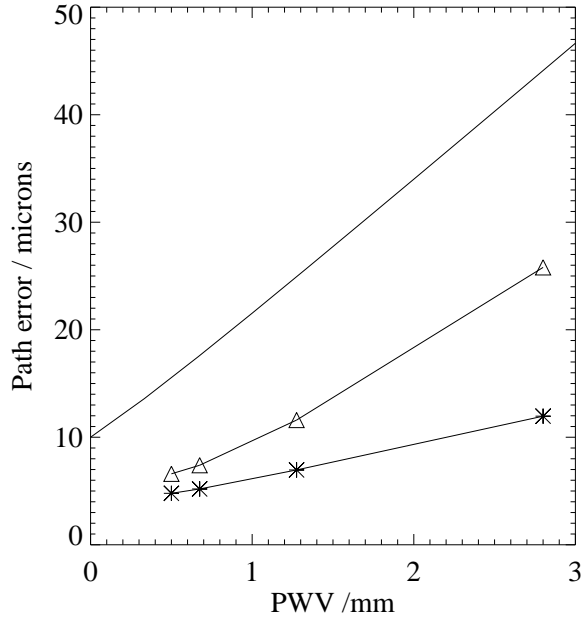


Figure 12: The predicted uncertainty in path length for a total path length of  $400\mu\text{m}$ . Stars take account only of radiometer noise (equation 15) and triangles include the  $dT/dL$  uncertainties (equation 18), with adjustments to the weights to minimise this error (table 5). The solid line shows the error specification (given by  $\{[10(1 + \text{PWV})]^2 + [0.02\Delta L]^2\}^{1/2}\mu\text{m}$ ).

## 6 The effect of hydrometeors on the path measurements

### 6.1 Ice

In this section we look at the expected performance of the WVR's in the presence of ice and liquid water hydrometeors in the atmosphere. While ice is not expected to affect the atmospheric refractive index significantly, if it contributes to the radiometric brightness temperature, it is likely to change the sensitivity parameter,  $dT/dL$ . It is therefore worth exploring how ice affects the brightness temperatures, and whether its presence can be detected by the WVR's. We have used the ATM to calculate brightness temperatures in the presence of ice particles (and in the next section water droplets), and details of the ATM modelling of hydrometeors can be found in Wiedner *et al.* (2004).

Ice scattering depends on the shape and alignment of the ice crystals as well as their size. For this work, we have assumed that the dominant source of ice crystals at the Chajnantor site is through orographic lifting of supersaturated air. This tends to generate spherical ice particles, since they are formed by freezing existing water droplets, with little subsequent accretion, and typically they have sizes around  $75\mu\text{m}$  (*e.g.* Scorer, 1997). Ice crystals formed as part of a cloud system tend to be larger, with typical sizes of  $250\mu\text{m}$  and a density of about  $0.025\text{ g m}^{-3}$  over a  $1.5\text{ km}$  layer (Dowling & Radke; 1990), (this corresponds to about  $0.04\text{ mm}$  of column integrated water).

We first perform an experiment in which a layer of ice is incorporated between 1 and 2.5

km above the Chajnantor site, with ice water amount ranging between 0.05 and 0.15 mm, and radii of 100 and 200  $\mu\text{m}$ . Figure 13 shows how the brightness temperature around the 183 GHz water line is changed by the presence of the ice. While 0.15 mm of crystals of radius 100  $\mu\text{m}$  change the brightness temperature by about 2 K, at 200  $\mu\text{m}$  the increase is closer to 12 K, showing that there is high sensitivity to particle size. The effect of the ice is two-fold – the first is to reduce the difference in brightness temperature between the wings of the water line profile and the maximum, and the second is to introduce additional asymmetry into the shape of the profile. While the first of these features is detectable with a double sideband radiometer, the second would only be detectable if the upper and lower sidebands can be separated, as is possible with a cross correlator radiometer.

The first effect can be detected by looking at the difference between pairs of radiometer channels (*i.e.* 1-4;2-4;3-4;2-3;1-3;1-2) and subtracting off the expected differences in the absence of ice. The asymmetry can be found by looking at the difference in brightness temperature between the upper and lower sidebands and again subtracting off the asymmetry in the absence of ice. Figure 14 shows these quantities for 100 and 200  $\mu\text{m}$  spherical ice crystals. While the cross channel values of  $\Delta T^{\text{BRI}}$  gives a larger signal, there is greater scope for confusion of this signal with other atmospheric conditions, for example water vapour distributions with a small scale height, which also act to reduce the height difference between the maximum and the wings of the profile.

In order to investigate whether sideband separation would be a useful property for the Chajnantor water vapour radiometers, it is worth calculating how much ice (and of what size) would have to be present in order for it to be detectable by the radiometer. We have used the radiometer equation to estimate the likely noise on brightness temperature estimates, which gives a limit to the sensitivity of the radiometer to the presence of asymmetry. We have then calculated the expected asymmetry for a grid of ice amounts and sizes, and plotted contours delineating levels of asymmetry that would be expected to be detectable at the 1,2 and 3  $\sigma$  level. Figure 15 shows that the sensitivity to ice is greatest when crystals have radius  $\sim 250\mu\text{m}$ , which is about  $\lambda/2\pi$  at the radiometer frequencies. This is what we might expect, since Mie theory predicts that the extinction cross section for spheres is at a maximum when the ratio of the particle circumference to the incident light wavelength is around unity. At 75  $\mu\text{m}$  the sideband-separating radiometer would be capable of detecting ice amounts greater than 0.04 mm to  $1\sigma$  and about 0.1 mm to  $2\sigma$  in channel 4.

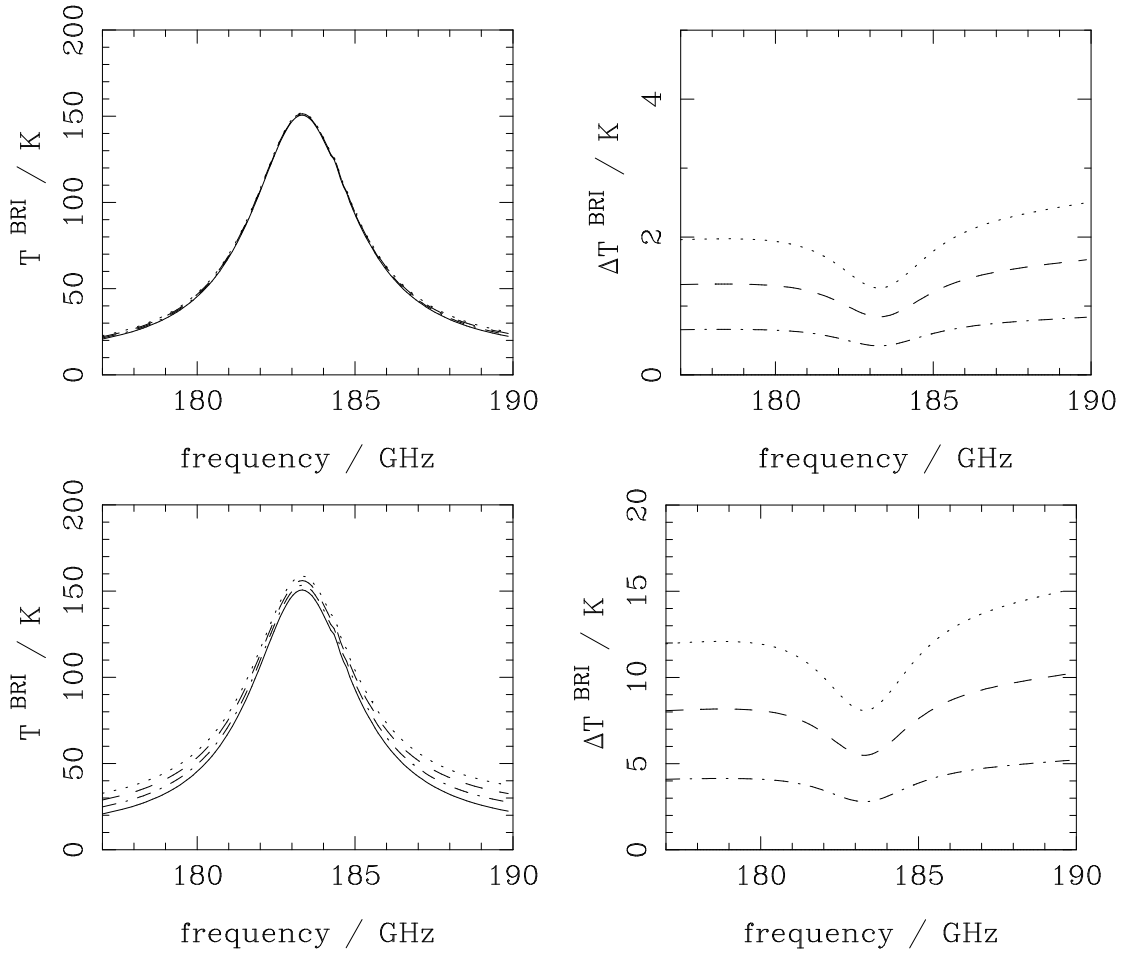


Figure 13: The impact of varying amounts of ice on brightness temperatures. The ice particles are spherical with radius 100 in the top panels, and 200  $\mu\text{m}$  in the bottom panels. Left panels show the brightness temperature, and right panels show the change in brightness temperature as a result of the ice (solid line is for no ice; dot-dashed for 0.05 mm of ice; dashed for 0.1 mm; and dotted for 0.15 mm).

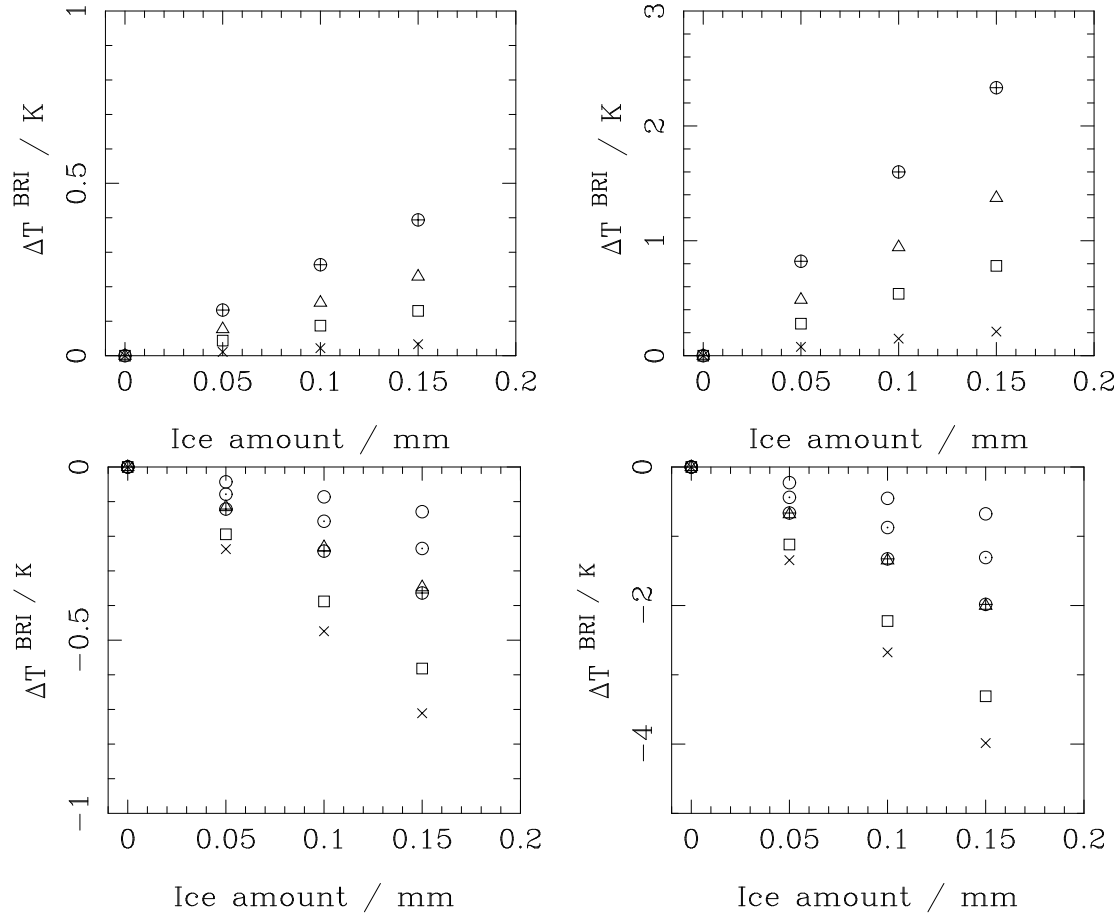


Figure 14: Top panels show the additional asymmetry between the upper and lower sideband channels compared with the no-ice case (crosses for channel 1, squares for channel 2, triangles for channel 3 and circles for channel 4). (left is for 100  $\mu m$ , and right for 200  $\mu m$ ). Bottom panels show a measure of the difference in brightness between the different channels (see text). (crosses: 1-4, squares 1-3, triangles 1-2, circles with + 2-4, dotted circles 2-3, open circles 3-4).

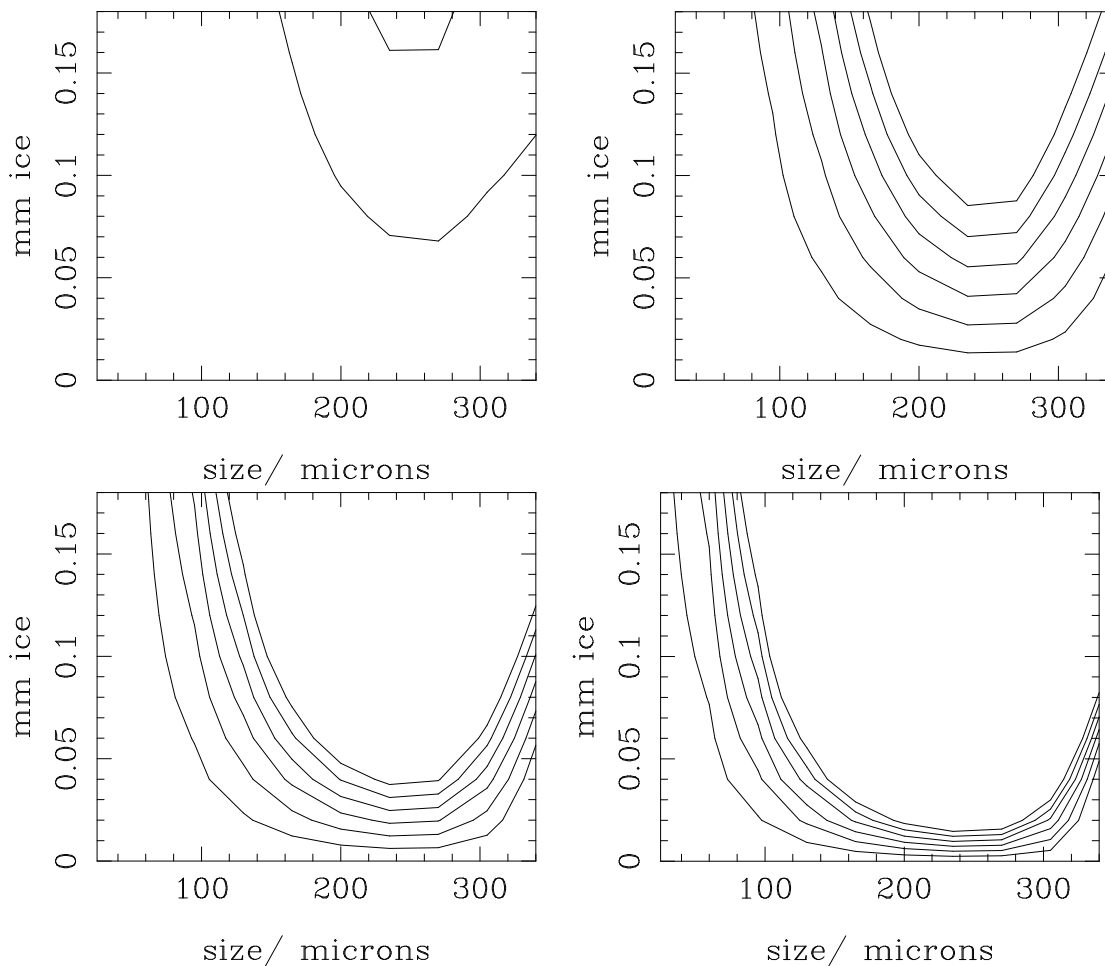


Figure 15: Contours showing the range of ice amounts and sizes that would be detectable by the radiometer channels. Top left is for channel 1; top right for channel 2; bottom left for channel 3 and bottom right for channel 4. Contour levels represent 1, 2, and 3 (4,5,6)  $\sigma$  errors expected from measuring the brightness temperature asymmetry. The asymmetry needs to be higher than the expected errors in order to be detectable.

## 6.2 Water droplets

Water droplets are also expected to produce an asymmetry in the 183 GHz line profile, and so we can apply the same approach to calculate the expected sensitivity to the presence of the droplets. Again, we assume that a likely source of water droplets is from lower altitude air being forced up onto the plateau, where it is cooled and the water vapour condenses to form fog. Water droplets in fog typically have sizes of  $5 - 30 \mu\text{m}$ , and concentrations of order 10 droplets per  $\text{cm}^3$  (*e.g.* Kunkel, 1971). We place the fog in a layer between 1 and 2.5 km above the ground for this study. Figure 16 shows how the brightness temperature changes with increasing number density of droplets each of size  $10 \mu\text{m}$ , and how the brightness temperature changes with size of droplets for a given amount of liquid water. Again the effect is to reduce the difference in brightness temperature between the maximum and the wings, and to introduce an asymmetry into the profile.

Figure 17 shows the asymmetry between the upper and lower sideband brightness temperatures for different liquid water amounts and droplet sizes. The asymmetry increases with water droplet concentration, but is relatively insensitive to droplet size. Again we can calculate how much liquid water would need to be present in order to be detectable by the radiometer, and figure 18 shows that the radiometer would be sensitive to amounts greater than  $0.002 \text{ mm}$  (which would correspond to a droplet concentration of just under 1 droplet per  $\text{cm}^3$ ).

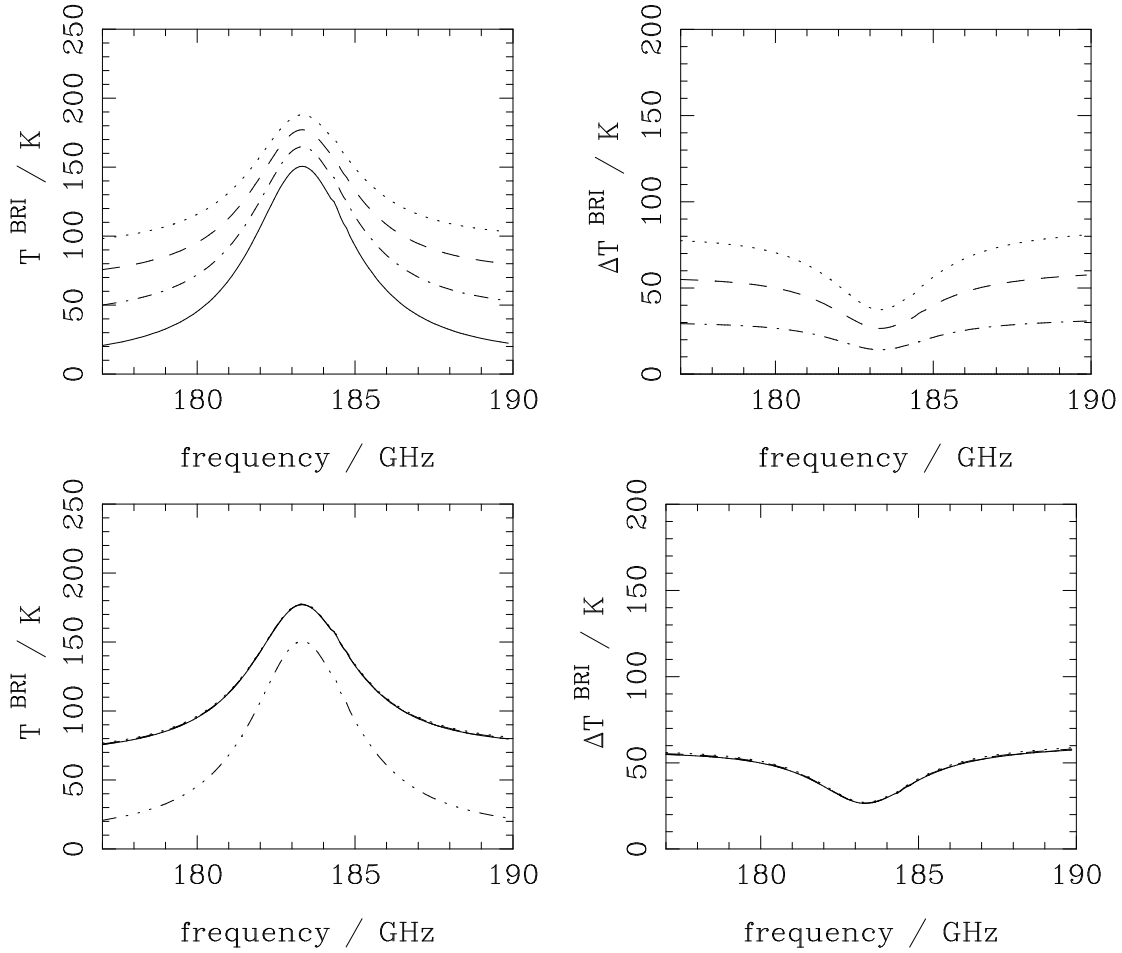


Figure 16: The impact of varying amounts of liquid water on brightness temperatures. Top panels show the effect of varying amounts of liquid water of droplet size  $10\mu\text{m}$  (solid line is for no liquid water; dot-dashed for 0.05 mm of droplets; dashed for 0.1 mm; and dotted for 0.15 mm), and bottom panels show the effect of varying the radius of the water droplets for an amount of 0.1 mm (solid is for 50  $\mu\text{m}$ ; dot-dashed for 100; dashed for 200; and dotted for 300  $\mu\text{m}$ , and dot-dot-dot-dashed is for no hydrometeor). Left panels show the brightness temperature, right panels show the change in brightness temperature as a result of the droplets.

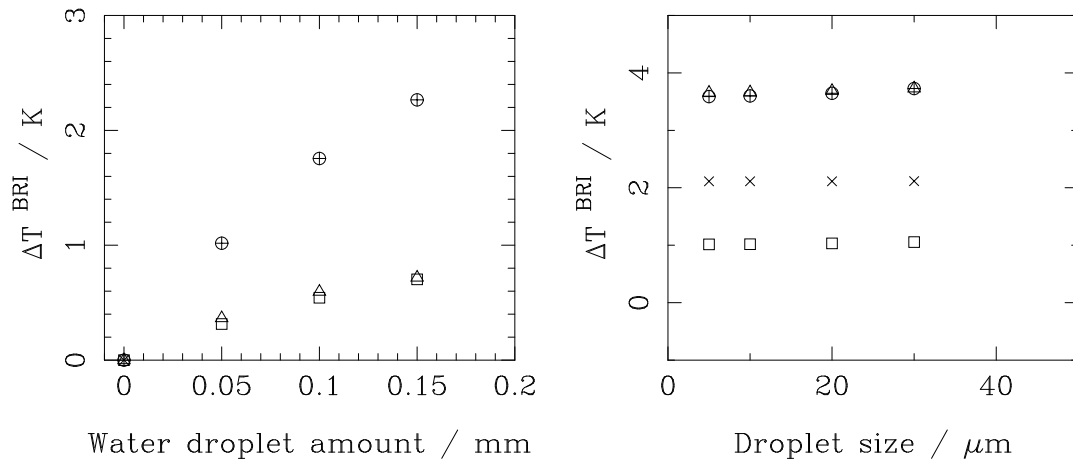


Figure 17: Left panel shows the additional asymmetry resulting from varying concentrations of water droplets of size  $10 \mu m$ . Right panel shows the asymmetry for varying sizes of water droplet and  $0.1 mm$  of liquid water. Crosses are for channel 1, squares for channel 2, triangles for channel 3 and circles for channel 4.

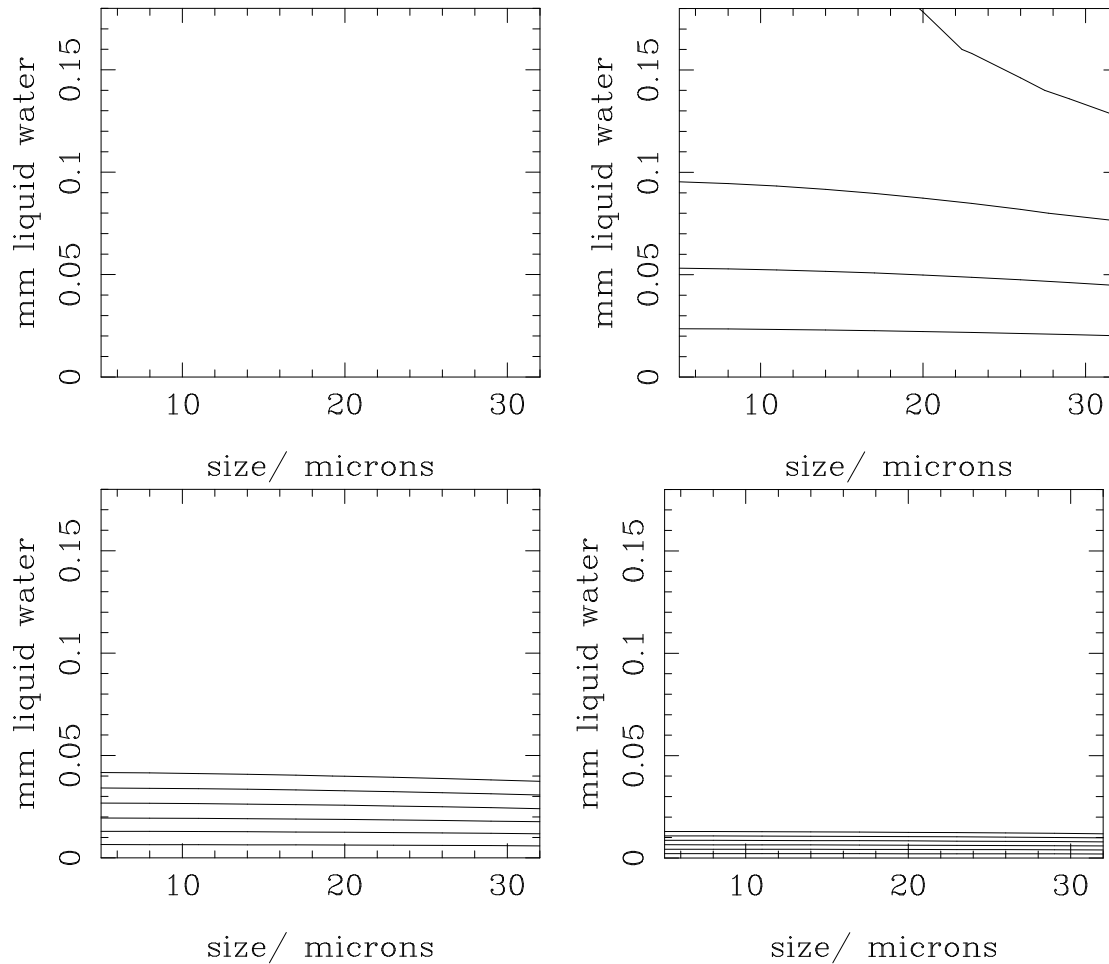


Figure 18: Contours showing the amount of liquid water expected to be detectable from a measurement of the asymmetry of the line profile. Top left is for channel 1 (nothing detectable in this channel) ; top right for channel 2; bottom left for channel 3; bottom right for channel 4.

## 7 Summary

In this report we have investigated the effect of changing atmospheric conditions on the radiometric sensitivity to path fluctuations. We have performed idealised experiments to model how quantities such as the water vapour scale height, the temperature profile, and the height of fluctuating water vapour influence the sensitivity. We have also measured the range of these properties from radiosonde data, and inferred a value for the uncertainty in the conversion factor between brightness temperature and path length of about 4% for PWV amounts of 1.275 mm or less. We have suggested how the four radiometer channels might be combined optimally to produce a best estimate for the path length, and find using this method a fractional path length error due to the atmosphere of about  $2\text{PWV}\%$ .

We have also investigated the influence of hydrometeors on the line profiles, focusing on the extent to which sideband separation might be used to detect the presence of ice or water droplets. We find that the Chajnantor radiometers could be sensitive to ice amounts over 0.02 mm, and water droplet amounts over  $10^{-3}$  mm if sideband separation is performed.

Future work on the wet fluctuations will concentrate on extending the error analysis to the case where PWV is not known exactly, and where vapour fluctuations are no longer confined to a single layer. The amplitude of dry fluctuations under varying atmospheric conditions should also be considered. Since there is scope for improving path variation estimates with additional calibration devices at the site such as a temperature profiler, it will also be worth evaluating how much these can be expected to assist our estimates of the path length.

## 8 References

- Carilli, C.L. & Holdaway, M.A., 1999, ALMA memo 262, ‘Tropospheric Phase Calibration in Millimeter Interferometry’
- Carilli, C.L., Lay, O.P., & Sutton, E.C., 1998, ALMA memo 210, ‘Radiometric phase correction’
- Delgado, G., Otárola, Nyman, L-A. *et al.* 2000, ALMA memo 332, ‘Phase correction of interferometer data at Mauna Kea and Chajnantor’
- Delgado, G., 2001, ALMA memo 361, ‘Phase Cross-Correction of a 11.2 GHz Interferometer and 183 GHz Water Line Radiometers at Chajnantor’
- Dowling, D.R., Radke, L., 1990, Journal of Applied Meteorology, Vol 29, 970, ‘A summary of the physical properties of cirrus clouds’
- Evans, N., Richer, J., Sakamoto, S., Wilson, C., Mardones, D., Radford, S., Cull, S., Lucas, R., 2003, ALMA memo No. 471, ‘Site Properties and Stringency’
- Hills, R.E., 2004, ALMA memo 495, ‘Estimated Performance of the Water Vapour Radiometers’
- Holdaway, M.A., 2001, ALMA memo 403 ‘Fast Switching Phase Correction Revisited for 64 12 m Antennas’

Holdaway, M.A., Pardo, J.R., 2001, ALMA memo 404, 'Atmospheric dispersion and fast switching phase calibration'.

Kunkel, Bruce A., 1971, Journal of Applied Meteorology Vol. 10, No. 3, pp. 482-486. 'Fog Drop-Size Distributions Measured with a Laser Hologram Camera.'

Lay, O.P., 1998, ALMA memo 209, '183 GHz Radiometric Phase Correction for the Millimeter Array'

Pardo, J.R., Cernicharo, J., Serabyn, E., 2001, IEEE Transactions on Antennas and Propagation, Vol. 49, No. 12. 1683

Radford, S., Butler, B., Otárola, A., et al, 2003  
<http://www.tuc.nrao.edu/mma/sites/Chajnantor/instruments/radiosonde/>

Robson, Y. et al, 2001, ALMA memo 345, 'Phase Fluctuation at the ALMA Site and the Height of the Turbulent Layer'

Scorer, R.E., 1997, Dynamics of Meteorology, John Wiley & Sons Inc, ISBN: 0471968153

Wiedner, M.C., Hills, R.E., Carlstrom, J.E., & Lay, O.P., 2001, ApJ 553, 1036.

Wiedner, M.C., Prigent, C., Pardo, J.R., Nuissier, O., Chaboureau, J-P., Pinty, J-P., Mascart, P., 2004, Journal Geophys. Res, Vol. 109, No. D6, D06214, 'Modeling of passive microwave responses in convective situations using output from mesoscale models: Comparison with TRMM/TMI satellite observations'

Yun, M.S. & Wiedner, M.C., 1999, ALMA memo 252, 'Phase Correction using 183 GHz Radiometers during the Fall 1998 CSO-JCMT Interferometer Run'